

Discovery of the Inner Ring around PSR B1509–58

Yoichi YATSU, Nobuyuki KAWAI

Department of Physics, Tokyo Institute of Technology, 2-12-1 Ookayama Meguro Tokyo 152-8551
yatsu@hp.phys.titech.ac.jp, nkawai@phys.titech.ac.jp

Shinpei Shibata

Department of Physics, Yamagata University, Yamagata 990-8560

and

Wolfgang Brinkmann

Max-Planck-Institut für Extraterrestrische Physik, Postfach 1603, 85740 Garching, Germany

(Received ; accepted)

Abstract

A *Chandra* study of pulsar wind nebula around the young energetic pulsar PSR B1509–58 is presented. The high resolution X-ray image with total exposure time of 190 ks reveals a ring like feature 10" apart from the pulsar. This feature is analogous to the inner ring seen in the Crab nebula and thus may correspond to a wind termination shock. The shock radius enables us to constrain the wind magnetization, $\sigma \geq 0.01$. The obtained σ is one order of magnitude larger than that of the Crab nebula. In the pulsar vicinity, the southern jet appears to extend beyond the wind termination shock, in contrast to the narrow jet of the Crab. The revealed morphology of the broad jet is coincident with the recently proposed theoretical model in which a magnetic hoop stress diverts and squeezes the post-shock equatorial flow towards the poloidal direction generating a jet.

Key words: ISM: jets and outflows — ISM: individual (G320.4–01.2) — ISM: supernova remnants — stars: pulsars: individual (PSR B1509–58) — X-rays: ISM

1. Introduction

Recent X-ray observations revealed that part of pulsar wind nebulae (PWNe) have common structures of “Torus” and “Jet”, as typified by the crab pulsar (Hester et al. 2002; Weisskopf et al. 2000), the Vela pulsar (Pavlov et al. 2003; Helfand et al. 2001), and PSR B1509–58 (Gaensler et al. 2002). However the physical mechanisms which form the ubiquitous features, especially the jets, are still unclear, because the origin of the jet in the Crab is too compact to discriminate its structure even with the current X-ray observatories.

The theoretical approaches toward the axisymmetric PWNe have been aimed to figure out the Crab nebula. The torus in the Crab had been successfully explained by one-dimensional MHD simulations (Kennel and Coroniti 1984a; Kennel and Coroniti 1984b). A young rotation powered pulsar is believed to lose its rotating energy via a magnetized particle flow from a pulsar, the so-called pulsar wind. Since the pulsar wind is flowing almost at the speed of light, it is stalled by a termination shock just around the pulsar. When the wind passes through the termination shock, the kinetic energy of the wind is converted into internal energy. Essentially, the post-shock flow is decelerated yielding to the conservation law of particle flux $nvr^2 = \text{const}$, where n is the number density (that is almost constant), v is the flow velocity and r is the radius from the pulsar. At the same time, the frozen-in condition, $rvB = \text{const}$, induces the compression of the toroidal magnetic field B , in which the internal energy

is efficiently converted into synchrotron radiation forming an X-ray torus.

In practice the magnetic pressure prevents the deceleration of the post-shock flow, thus the magnetization of the pulsar wind is closely related to the geometric structure of the PWN. In this way, several methods to calculate the magnetization parameter σ have been proposed (Rees and Gunn 1974; Kennel and Coroniti 1984a; Gallant and Arons 1994). Moreover, recent two-dimensional numerical studies suggested that the magnetization seems to control the formation of the jet (Lyubarsky 2002; Del Zanna et al. 2004; Bucciantini 2006). Therefore it is essential to evaluate the magnetization parameters to understand the formation process of PWNe.

So far, the shock front of the pulsar wind has been observed only in the Crab nebula (Weisskopf et al. 2000) because of the small angular sizes of PWNe. Nevertheless the *Chandra* X-ray observatory with sub-arcsec-scale spatial resolution has the potential to detect the wind termination shocks in other PWNe. In order to obtain a general understanding of the formation process of PWNe, we investigate the fine structures around the pulsar PSR B1509–58 utilizing the *Chandra* data.

PSR B1509–58 is emitting 150 ms radio, X-ray, and Gamma-ray pulsation (Seward and Harnden 1982; Manchester et al. 1982; Ulmer et al. 1993). From the spin parameters, a characteristic age $\tau_c = 1700$ yr, a spin-down luminosity $\dot{E} = 1.8 \times 10^{37}$ ergs s^{-1} , and a surface magnetic field $B_p = 1.5 \times 10^{13}$ G have been obtained, making it one of the youngest, the most energetic, and highest field

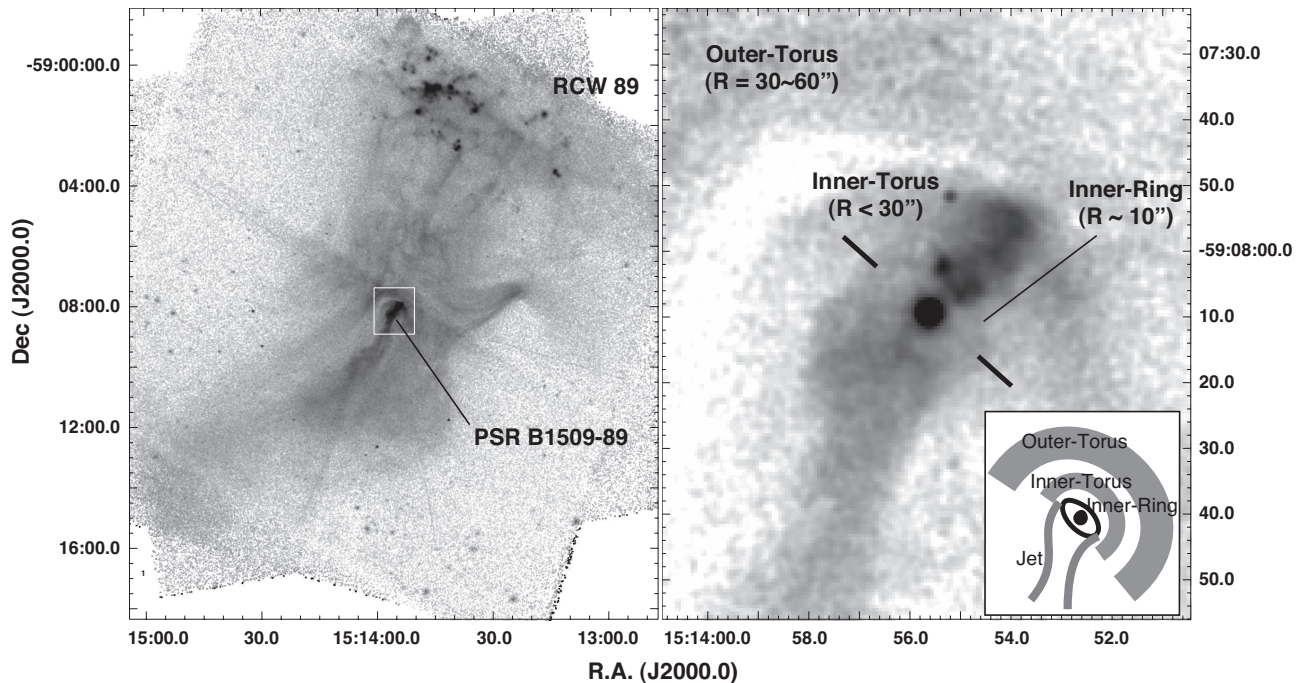


Fig. 1. (Left)— Overview image of the PWN accompanied by PSR B1509–58 with 190 ks exposure taken by *Chandra*. The image was smoothed with a Gaussian of $\sigma = 2.0''$. The white rectangle indicates the FoV of the right panel. (Right)— Close-up image of the pulsar vicinity smoothed with a Gaussian of $\sigma = 0.5''$. The inner panel schematically describes the remarkable structures.

pulsars known (Seward and Harnden 1982; Kaspi et al. 1994). The pulsar is accompanied by a bright and large PWN with remarkable jet-like features extending to the southeast and northwest (Gaensler et al. 2002).

The pulsar and its PWN appears to be embedded in a 30 arcmin radio shell G320.4–01.2 (Caswell et al. 1981). An HI observation yielded the distance of $d = 5.2 \pm 1.4$ kpc from the earth (Gaensler et al. 1999). Adopting this distance and standard parameters of the ISM and supernova explosions yields an age of 6–20 kyr, which is one order of magnitude larger than the pulsar’s characteristic age (Seward et al. 1983).

Moreover Yatsu et al. (2006) detected proper motions of X-ray clumps in RCW 89 which coincide with the north radio shell from the 4.3 yr base-line *Chandra* observations. These results imply that the pulsar and the SNR have the same progenitor in a cavity. If this is the case the termination shock of the pulsar wind can be easily discriminated by *Chandra*.

The paper is structured as follows. The *Chandra* observations and their results are shown in §2. The imaging analysis and spectral analysis are described in §3 and §4, respectively. Finally, we discuss the obtained results in §5.

2. Observations

The vicinity of PSR B1509–58 has been observed several times by the *Chandra* X-ray Observatory. For this study, the four most recent observations which are sequentially performed from 2004 to 2005 are utilized. The

exposure time of the each observation is about ~ 50 ks. The aiming point (ACIS-I) was set on ($15^{\text{h}}13^{\text{m}}55^{\text{s}}60$, $-59^{\circ}08'08''.9$). The observational settings are summarized in Table 1.

We have performed the reduction process for the each data set using “*acis_event_process*” in CIAO version 4.0. Although these four observations are performed in VFaint-Mode, we applied standard background cleaning using 3×3 event island, because the VFaint-Mode background cleaning process tends to misjudge a certain amount of source photons to be background events.

Figure 1 shows X-ray images combining the four *Chandra* observations. Thanks to the long exposure time of 190 ks, several fine structures are revealed. The pulsar wind nebula is very large, almost filling the radio shell of G320.4–01.2. The length of the X-ray nebula along the jet-like feature reaches $\sim 16'$, which corresponds to ~ 24 pc for the distance $d = 5.2$ kpc. The south edge of the nebula is more distant ($\sim 10'$) from the pulsar than the north edge ($\sim 6'$), while the width of the nebula across the east-west direction is about $8'$, which is a half of the length along the axis.

Interestingly the western side of the PWN appears to be sharply cut off at $2'$ from the pulsar, implying that the pulsar wind is confined by an invisible ISM. Moreover filament-like absorption features are seen at the western edge. Evidently, the column density seems to change at these features (Yatsu 2008). A more detailed treatment and discussion of these data are deferred to a subsequent paper.

In the close-up image in Figure 1, nested triplet ring

features, which are labeled “Outer-Torus”, “Inner-Torus”, and “Inner-Ring”, are found. The outer features have already been reported by Gaensler et al. (2002). The outer torus is seen at a separation of $\sim 60''$ from the pulsar. In the inner side of the outer-torus, an inner-torus with a radius of $\sim 30''$ exists. Most intriguing is an indication of an “Inner-Ring” structure $\sim 10''$ apart from the pulsar as seen in the Crab nebula (Weisskopf et al. 2000). Nevertheless the existence of the ring feature is still ambiguous comparing with the Crab, which might be due to the contamination from the bright nebula core.

3. Data Analysis and Results

3.1. Imaging analysis

In order to visualize the compact structures in the vicinity of the pulsar, we applied an “unsharp mask”, which is a kind of the high-pass filter, to the *Chandra* image. First, we generated a low-frequency component image that should be removed. To avoid the impact from the bright point sources such as the pulsar, we removed noticeable point sources using “wavdetect” in CIAO 4.0. The gap regions were extrapolated from the surrounding areas using “dmfilth”. Then the filled-in image was normalized by the exposure map. Finally, the exposure corrected image was smoothed using the tool “aconvolve”. As a convolution kernel, a Gaussian function of $\sigma = 3.5''$ was adopted. We also generated a source image by the same method as for the low-frequency image but with a smoothing with a Gaussian of $\sigma = 0.5''$. Finally, the low-pass filtered component was subtracted from the source image.

The resultant image is shown in Figure 2. The inner ring is clearly distinguished from the pulsar. The radius of the ring feature appears to be $\sim 10''$ along the major axis, that corresponds to 7.8×10^{17} cm for the distance of 5.2 kpc from earth. The eccentricity of $\epsilon \sim 0.8$, for a minor axis radius of $\sim 6''$, implies an inclination angle of $i \sim 50^\circ$ which is somewhat smaller than that from the appearance of the outer torus (Gaensler et al. 2002). On the north edge of the inner ring, there are emitting blobs, which forms the north jet. These small structures are seen only in the north side of the pulsar, while the south jet appears to be diffuse. The south jet across the flow line is about $20''$ at the origin, which just corresponds to the radius of the ring feature. These structures seems to changes temporally (Yatsu 2008). The detailed temporal analysis will be reported in a subsequent paper.

Next we measure the radius of the ring feature based

Table 1. Summary of the observations of PSR B1509–58.

ObsID#	Date	Detector	Mode	Exposure (s)
5534	2004/12/28	ACIS-I	VFaint	50130
5535	2005/02/07	ACIS-I	VFaint	43130
6116	2005/04/29	ACIS-I	VFaint	47650
6117	2005/10/18	ACIS-I	VFaint	46140

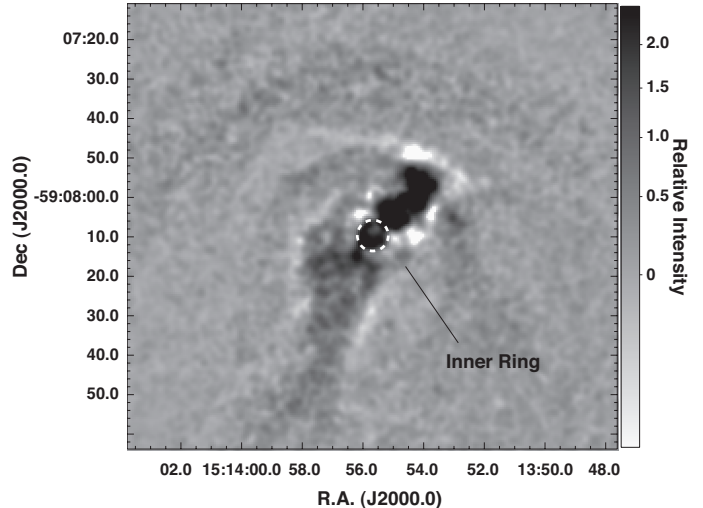


Fig. 2. Unsharp masked image of the pulsar vicinity. This image was generated from a source image smoothed with a Gaussian of $\sigma = 0.5''$, from which a low-pass image smoothed with a Gaussian of $\sigma = 3.5''$ was subtracted. The pulsar’s location is indicated by the white dashed-line.

on the radial profile of the surface brightness for a quantitative discussion. As shown in Figure 3, sixty sub-regions were selected from which the X-ray photons were accumulated. Each of the sub-regions has a width of $1.0''$. The ellipticity of the regions are aligned with the inner-ring. In order to exclude the jet components, the north-west quadrant and the south-east quadrant respect to the pulsar were masked. Thus the resultant sub-regions exhibit bow-tie shapes.

The radial profile of the X-ray surface brightness for 0.4~8.0 keV band is shown in Figure 4. The error bars indicate the statistical uncertainties corresponding the total numbers of the X-ray photons detected at the each sub-region. Since a sub-region accumulates more than 1000 photons, the relative uncertainty is smaller than $\sim 4\%$.

To constrain the radius of the ring feature, we performed a model fitting with a multi-component function consisting of two power-law functions and a Gaussian function. For the fitting we utilized the data points ranged in $2''.0 \sim 28''.0$. The centroid of the Gaussian that corresponds to the inner ring was $9''.0 \pm 0''.1$ at 1σ confidence level. The other parameters are summarized in Table 2.

3.2. Spectral analysis

In this section the spatially resolved spectroscopy is presented. Since the photon statistics was a little poor, we investigated the spectral evolution with a spatial resolution of $3''$. The examined regions are the north-east side of the bow-tie shape in Figure 3.

For the model fittings, we employed a single component model consisting of an absorbed power-law function. However, it is difficult to determine the column density for each region individually, because the source regions are small. Therefore we fixed the column density

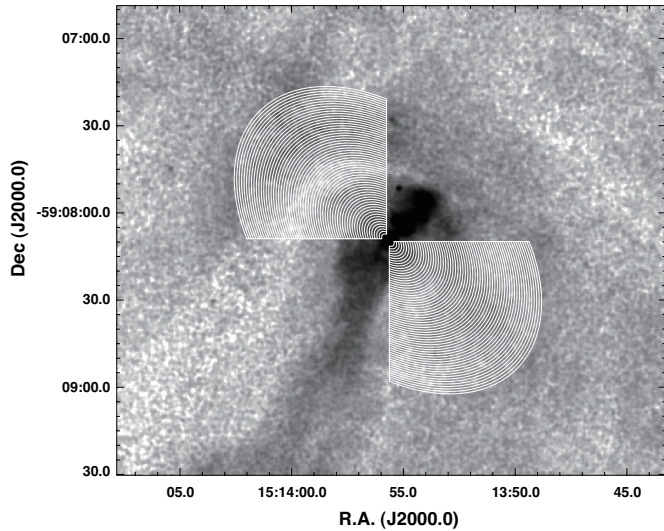


Fig. 3. The sub-regions to be analyzed are described by white lines. The each sub-region has a width of $1''.0$ along the major axis (North-east~South-west).

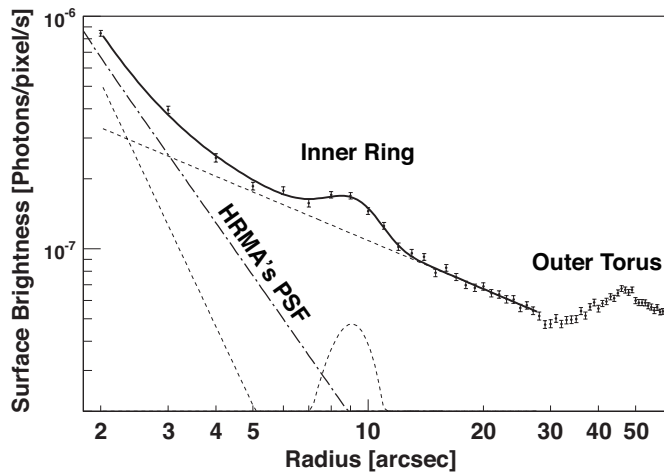


Fig. 4. The radial profile of the X-ray surface brightness at the energy band 0.4-8.0 keV. The solid line shows the model function consists of a Gaussian function and two power-law functions. The dashed lines show the each component consisting the model. The dot-dash line shows HRMA's point spread function normalized by the pulsar's luminosity at $1''$ from the pulsar.

at $N_{\text{H}} = 1.0 \times 10^{22} \text{ cm}^{-2}$. With the above configurations, the four data sets observed in the different epochs could not be explained by the same parameter set, the energy flux varies with time. These results may be caused by the temporal changes of the PWN or by the different settings of instrumentation, such as the roll angle. Thus we allowed the normalizations of the four data-sets to vary individually.

The results of model fittings are shown in Figure 5, indicating the evolution of the surface brightness and the photon index as a function of radius. In all panels, shapes of the data points correspond to the

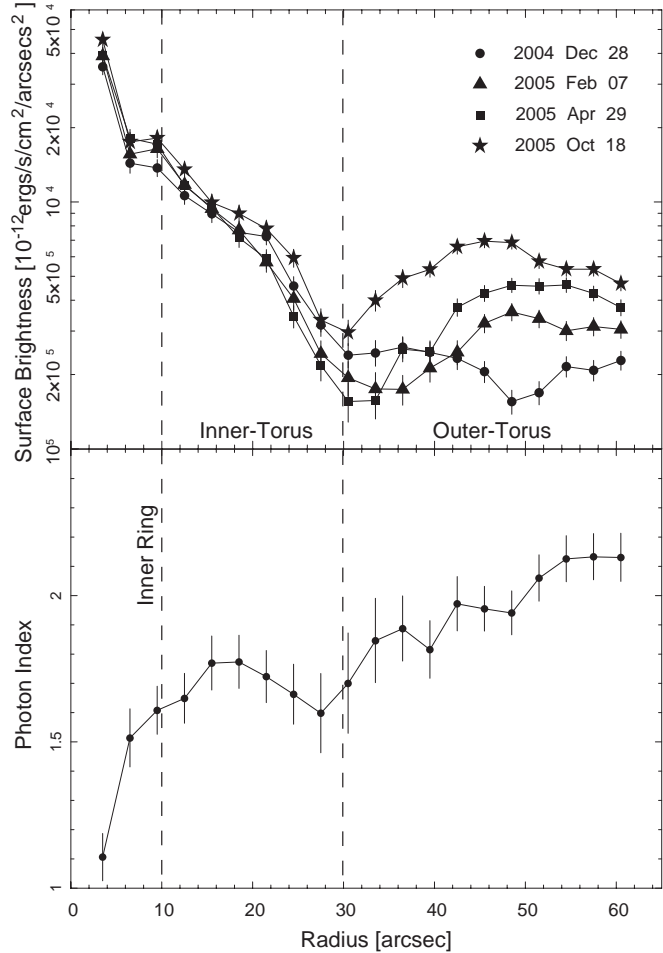


Fig. 5. The evolutions of the surface brightness (upper panel) and the photon index (lower-panel) are shown as functions of radius. The shape of the data points corresponds to the epochs, 2004-Dec-28 (circle), 2005-Feb-07 (triangle), 2005-Apr-29 (square), and 2005-Oct-18 (star).

epochs, 2004-Dec-28(circle), 2005-Feb-07(triangle), 2005-Apr-29(square), and 2005-Oct-18(star). The surface brightness slightly increases at a radius of $\sim 9''$, corresponding the inner ring. At $R \sim 30''$, the light curve shows a dip which corresponds to the gap between the inner torus and the outer-torus. The photon index seems to be constant in the inner torus within $R \sim 30''$, while it increases in the outer-torus outside the radius of $R \sim 30''$.

4. Discussion

4.1. Double tori

As shown in Figure 4, the PWN around PSR B1509-58 has a centrally concentrated surface brightness profile, which may be caused by its comparatively small angular size or the contamination from the bright jet structure pointing towards us. For this reason, it is difficult to compare the surface brightness evolution of PSR B1509-58 with that of the Crab nebula in a simple way. Nevertheless PSR B1509-58 possesses an apparently different mor-

phology; the nested double ring structure, inner-torus ($R \sim 30''$) and outer-torus ($30'' < R < 60''$), lying in the equatorial plane relative to the spin axis.

Spectroscopy, these two tori, calling the inner torus and the outer torus, seems to be completely different. The inner-torus has a constant photon index of $\Gamma \sim 1.6$ which is the same as that just at the pulsar. In contrast, the photon index in the outer-torus obviously increases with the radius from $\Gamma = 1.6$ to 2.1. The observed interval of the photon index variation is $\Delta\Gamma \sim 0.5$, which implies that the observed spectral evolution is caused by synchrotron cooling (Kardashev 1962).

In case of the Crab nebula, the post-shock photon index is $\Gamma = 2.1$ and it does not change within the torus. According to Kennel and Coroniti (1984a), the evolution of the surface brightness in the torus can be explained by the compression of the toroidal magnetic field, which enhances the synchrotron energy loss. Thus the bright torus of the Crab simply corresponds to the region in which most of the X-ray emitting particles radiate their energy and burn off there. Consequently the photon index outside of the torus is steeper than $\Gamma = 2.1$, and the surface brightness decays rapidly.

In terms of spectroscopy, the counterpart of the X-ray torus in the Crab is the inner torus rather than the outer torus of PSR B1509–58. While in the outer-torus the X-ray emitting charged particles have burnt off and thus the synchrotron cooling break is passing through the observed energy band (8.0 keV to 0.4 keV). Moreover, it was reported that the outer-torus has a radio counter part (Gaensler et al. 2002). These results of the spectroscopy imply that the outer-torus could not be simply explained by radiative losses as claimed by Gaensler et al. (2002).

4.2. Inner Ring

It is essential to know the radius of the pulsar wind termination shock to understand the mechanism which forms the structure of a PWN. So far, the termination shock of the pulsar wind has been observed only in the Crab nebula. In this section we discuss the ring feature discovered near around PSR B1509–58 comparing it with the inner ring of the Crab nebula.

As the pulsar wind is believed to be ejected almost at the light speed, the free flowing region should not be radiating as seen in the Crab nebula. In the case of PSR B1509–58 the region within the ring feature is also dark. Comparing it with the tori which are strongly affected by the Lorentz boost, the surface brightness of the ring feature appears to be uniform, so that we can distinguish the south edge of the ring. For the Crab nebula Weisskopf et al. 2000 pointed out that the surface brightness of the inner ring is more uniform in azimuth, indicating that relativistic beaming is less significant in it than in the torus. The observed apparent properties can distinguish the ring from the tori and then the hypothesis that the ring structure represents the termination shock can be suggested. By the way, the ring shows an obvious elliptic shape, implying that the shock front in an ellipsoidal surface or a ring viewed with inclination rather than a sphere.

Regarding the issue, recent numerical simulations predict a shock front with an oblate shape for an anisotropic pulsar wind (Komissarov and Lyubarsky 2003; Del Zanna et al. 2004).

At the termination shock, pressure balance between the ram pressure of the pulsar wind and the post-shock plasma is expected, as seen in the Crab nebula. Based on the X-ray image 2, we obtained a radius of the ring structure of $r \sim 9''$, which corresponds to 7×10^{17} cm for the distance of 5.2 kpc to the pulsar. Assuming that most of the pulsar's rotating energy, $\dot{E} = 1.8 \times 10^{37}$ ergs s^{-1} , is transferred to the relativistic pulsar wind at the light cylinder, we find the ram pressure of the pulsar wind at the ring structure to be

$$p_* = \frac{\dot{E}}{4\pi r_{\text{TS}}^2 \phi c} \quad (1)$$

$$= 9.6 \times 10^{-11} \phi^{-1} \left(\frac{d}{5.2 \text{ kpc}} \right)^{-2} \left(\frac{R}{9''.0} \right)^{-2} \text{ dyn cm}^{-2}$$

where ϕ is the fraction of a sphere covered by the wind.

On the other hand, the inner pressure of the nebula is roughly estimated by assuming equipartition conditions (Reference). From the spectral fits we obtained an X-ray flux of 1.32×10^{-13} ergs s^{-1} cm^{-2} and a photon index of $\Gamma = 1.6$ for the region where the ring feature exists ($R = 10''$) and we infer an unabsorbed luminosity density at 1 keV $L_{1 \text{ keV}} = 6.6 \times 10^{14}$ ergs s^{-1} Hz^{-1} . For simplification we assumed the emitting volume to be a partial spherical shell of radius $R = 10''$, thickness $\Delta R = 3''$ and opening angle of 45° , corresponding to $V = 2.6 \times 10^{53}$ cm^3 , which may be an overestimate. For a filling factor f and a ratio of ion to electron energy μ , the minimum energy present in the source responsible for the synchrotron emission $W_{\text{total}} \sim 2.9(1 + \mu)^{4/7} f^{3/7} \times 10^{43}$ ergs and a magnetic field of $B \sim 35(1 + \mu)^{2/5} f^{-2/7}$ μG are inferred. The corresponding pressure of the relativistic gas is then $p_{\text{neb}} = W_{\text{total}}/3V \sim 3.7(1 + \mu)^{3/7} f^{-4/7} \times 10^{-11}$ dyn cm^{-2} ¹. Note that the obtained inner pressure is a lower limit because the post-shock flow of a weakly magnetized pulsar wind is believed to be in particle dominant conditions rather than in equipartition (Kennel and Coroniti 1984a). Taking into account this fact, p_* and p_{neb} are comparable, implying that the ram pressure of the pulsar wind and the internal pressure of the PWN is balanced at the ring feature. It is therefore inferred that the newly found ring feature is the termination shock of the pulsar wind.

4.3. Magnetization of the pulsar wind

Adopting that the discovered ring feature corresponds to the wind termination shock, the magnetization parameter σ can be estimated. As the shock transforms the kinetic energy into thermal energy, σ can be rewritten as (Shibata et al. 1998)

¹ For a torus geometry with opening angle 15° corresponding to $f \sim 0.5$, the internal pressure of $p_{\text{neb}} \sim 5.6(1 + \mu)^{3/7} \times 10^{-11}$ dyn cm^{-2} can be obtained.

$$\sigma = \frac{B_1^2/4\pi}{[\text{kinetic energy density}]} \quad (3)$$

$$\sim \frac{B_1^2/4\pi}{[\text{postshock thermal energy density}]} \quad (4)$$

$$\sim \frac{B_1^2/4\pi}{B_{\text{Eq}}^2/4\pi}, \quad (5)$$

where B_1 is the toroidal magnetic field just behind the shock, and E_{Eq} is the equipartition magnetic field after the shock. Combining this equation with the equation of continuity ($r_{\text{TS}}^2 c/3 = r_n^2 v_n$) and the flux conservation law ($r_{\text{TS}} c B_1 = r_n B_{\text{Eq}}$) yields

$$\frac{r_n}{r_{\text{TS}}} \sim \frac{1}{3\sqrt{\sigma}}. \quad (6)$$

Substituting a shock radius $r_{\text{TS}} = 9''$ and a radius of the nebula $r_n = 30''$, corresponding to the inner-torus, we obtain $\sigma \sim 0.01$, which is twice larger than that reported by Gaensler et al. (2002) although they regarded the inner-torus in Figure 1 as a wind termination shock.

In case of the Crab nebula a magnetization parameter of $\sigma = 0.003$ based on the expansion velocity was calculated by Kennel and Coroniti (1984a), while Mori 2002 also reported a larger magnetization parameter of $\sigma \sim 0.03$ based on imaging analyses utilizing *Chandra*.

4.4. South jet

The south jet in the pulsar vicinity is remarkably different from that seen in the Crab. In case of the Crab nebula, the jet seems to flow out directly from the pulsar, even *Chandra* cannot resolve the origin of the jet (Weisskopf et al. 2000; Hester et al. 2002; Mori et al. 2004). In contrast, the jet of PSR B1509–58 extends over $\sim 10''$ at the origin. Also, the jet itself is broad and brighter than its torus. If the newly discovered ring feature is a wind termination shock, the south jet of PSR B1509–58 may flow out from the vicinity of the shock front or from the inner-torus, namely the post shock region.

The appearance of the south jet at the origin seems to match the recent theoretical scenario in which the hoop stress in the pulsar wind collimates the poloidal flow (Lyubarsky 2002). This idea was of course introduced for the Crab nebula, however, it is difficult to explain the narrow jet because the magnetic pinch works well only downstream of the shock. Downstream, the magnetic hoop stress is believed to be able to squeeze the “mildly relativistic” flow towards the rotating axis. The observed features indicate that this model can be applied to PSR B1509–58.

Del Zanna et al. (2004) reported two dimensional relativistic MHD simulations of pulsar jets in various configurations. Interestingly the observed morphology of the PWN around PSR B1509–58 closely resembles the results of the simulations for $\sigma = 0.03$. They argued that producing a jet by magnetic hoop stress requires a comparatively large magnetization parameter, $\sigma \geq 0.01$, which is coincident with the calculated value shown above. It is therefore argued that the south jet of PSR B1509–58 originates in the post-shock equatorial flow.

References

- J. J. Hester, K. Mori, D. Burrows, J. S. Gallagher, J. R. Graham, M. Halverson, A. Kader, F. C. Michel, and P. Scowen, *ApJL* **577**, L49–L52 (2002).
- M. C. Weisskopf, J. J. Hester, A. F. Tennant, R. F. Elsner, N. S. Schulz, H. L. Marshall, M. Karovska, J. S. Nichols, D. A. Swartz, J. J. Kolodziejczak, and S. L. O’Dell, *ApJL* **536**, L81–L84 (2000), [arXiv:astro-ph/0003216](#).
- G. G. Pavlov, M. A. Teter, O. Kargaltsev, and D. Sanwal, *ApJ* **591**, 1157–1171 (2003), [astro-ph/0305510](#).
- D. J. Helfand, E. V. Gotthelf, and J. P. Halpern, *ApJ* **556**, 380–391 (2001), [astro-ph/0007310](#).
- B. M. Gaensler, J. Arons, V. M. Kaspi, M. J. Pivovarov, N. Kawai, and K. Tamura, *ApJ* **569**, 878–893 (2002), [astro-ph/0110454](#).
- C. F. Kennel, and F. V. Coroniti, *ApJ* **283**, 694–709 (1984a).
- C. F. Kennel, and F. V. Coroniti, *ApJ* **283**, 710–730 (1984b).
- M. J. Rees, and J. E. Gunn, *MNRAS* **167**, 1–12 (1974).
- Y. A. Gallant, and J. Arons, *ApJ* **435**, 230–260 (1994).
- Y. E. Lyubarsky, *MNRAS* **329**, L34–L36 (2002).
- L. Del Zanna, E. Amato, and N. Bucciantini, *A&A* **421**, 1063–1073 (2004), [arXiv:astro-ph/0404355](#).
- N. Bucciantini, “Modeling Pulsar Wind Nebulae,” in *36th COSPAR Scientific Assembly*, 2006, vol. 36 of *COSPAR, Plenary Meeting*, pp. 191–+.
- F. D. Seward, and F. R. Harnden, Jr., *ApJL* **256**, L45–L47 (1982).
- R. N. Manchester, I. R. Tuohy, and N. Damico, *ApJL* **262**, L31–L33 (1982).
- M. P. Ulmer, S. M. Matz, R. B. Wilson, M. J. Finger, K. S. Hagedorn, D. A. Grabelsky, J. E. Grove, W. N. Johnson, R. L. Kinzer, J. D. Kurfess, W. R. Purcell, M. S. Strickman, V. M. Kaspi, S. Johnston, R. N. Manchester, A. G. Lyne, and N. D’Amico, *ApJ* **417**, 738–+ (1993).
- V. M. Kaspi, R. N. Manchester, B. Siegman, S. Johnston, and A. G. Lyne, *ApJL* **422**, L83–L86 (1994).
- J. L. Caswell, D. K. Milne, and K. J. Wellington, *MNRAS* **195**, 89–99 (1981).
- B. M. Gaensler, K. T. S. Brazier, R. N. Manchester, S. Johnston, and A. J. Green, *MNRAS* **305**, 724–736 (1999), [astro-ph/9901262](#).
- F. D. Seward, F. R. Harnden, Jr., P. Murdin, and D. H. Clark, *ApJ* **267**, 698–710 (1983).
- Y. Yatsu, N. Kawai, J. Kataoka, K. Tamura, and W. Brinkmann, *The X-ray Universe* pp. 379–380 (2006).
- Y. Yatsu, *Study of Pulsar Wind Nebulae with Chandra*, Ph.D. thesis, Tokyo Institute of Technology. (2008).
- N. S. Kardashev, *Soviet Astronomy* **6**, 317–+ (1962).
- S. S. Komissarov, and Y. E. Lyubarsky, *MNRAS* **344**, L93–L96 (2003), [arXiv:astro-ph/0306162](#).
- S. Shibata, N. Kawai, and K. Tamura, “Pulsar Nebulae as Calorimeters,” in *Neutron Stars and Pulsars: Thirty Years after the Discovery*, edited by N. Shibazaki, 1998, pp. 457–+.
- K. Mori, *An X-ray study of the Crab Nebula with Chandra*, Ph.D. thesis, Osaka Univ. (2002).
- K. Mori, D. N. Burrows, J. J. Hester, G. G. Pavlov, S. Shibata, and H. Tsunemi, *ApJ* **609**, 186–193 (2004), [astro-ph/0403287](#).

Table 2. Summary of the model fitting of the radial profile.

Parameter.....	Value
Gaussian	
Normalization.....	$4.76 \pm 0.44 (\times 10^{-8} \text{ photons s}^{-1} \text{ pixel}^{-1})$
Mean.....	$9''.06 \pm 0''.14$
Sigma.....	$1''.48 \pm 0''.18$
Power-law (1)	
Normalization.....	$5.36 \pm 0.65 (\times 10^{-7} \text{ photons s}^{-1} \text{ pixel}^{-1})$
Index.....	-0.69 ± 0.04
Power-law (2)	
Normalization.....	$5.82 \pm 1.31 (\times 10^{-6} \text{ photons s}^{-1} \text{ pixel}^{-1})$
Index.....	-3.48 ± 0.37

The quoted uncertainties are 1σ .